Evaluation of GEOS Precipitation Flagging for SMAP Soil Moisture Retrieval Accuracy

Maheshwari Neelam[1,2], Rajat Bindlish[1], Peggy O'Neill[1], George J. Huffman[3], Rolf Reichle[4], Steven Chan[5], Andreas Colliander[5]

Submitted

Journal of Hydrometeorology

[1] Hydrological Sciences Laboratory, NASA Goddard Space Flight Center, Greenbelt, MD 20771, USA
[2]Science Systems & Applications Inc, Lanham, MD 20706, USA
[3]Mesoscale Atmospheric Processes Laboratory, NASA Goddard Space Flight Center, Greenbelt, MD 20771, USA
[4]Global Modeling and Assimilation Office, NASA Goddard Space Flight Center, Greenbelt, MD 20771, USA
[5]NASA Jet Propulsion Laboratory, California Institute of Technology, Pasadena, CA 91109, USA
*Corresponding Author: maheshwari.neelam@nasa.gov

Evaluation of GEOS Precipitation Flagging for SMAP Soil Moisture Accuracy

Maheshwari Neelam[1,2], Rajat Bindlish[1], Peggy O'Neill[1], George J. Huffman[3], Rolf Reichle[4], Steven Chan[5], Andreas Colliander[5]

[1]NASA Goddard Space Flight Center, Greenbelt, MD 20771, USA
[2]Science Systems & Applications Inc, Lanham, MD 20706, USA
[3]Mesoscale Atmospheric Processes Laboratory, NASA Goddard Space Flight Center, Greenbelt, MD 20771, USA
[4]Global Modeling and Assimilation Office, NASA Goddard Space Flight Center, Greenbelt, MD 20771, USA
[5]NASA Jet Propulsion Laboratory, California Institute of Technology, Pasadena, CA 91109, USA

Abstract

The precipitation flag in the Soil Moisture Active Passive (SMAP) Level 2 passive soil moisture (L2SMP) retrieval product indicates the presence or absence of heavy precipitation at the time of the SMAP overpass. The flag is based on precipitation estimates from the Goddard Earth Observing System (GEOS) Forward Processing numerical weather prediction system. An error in flagging during an active or recent precipitation event can either (1) produce an overestimation of soil moisture due to short-term surface wetting of vegetation and/or surface ponding (if soil moisture retrieval was attempted in the presence of rain), or (2) produce an unnecessary non-retrieval of soil moisture and loss of data (if retrieval is flagged due to an erroneous indication of rain). Satellite precipitation estimates from the Integrated Multi-satellite Retrievals for GPM (IMERG) Version 06 Early Run (latency of ~4 hrs) precipitationCal product are used here to evaluate the GEOS-based precipitation flag in the L2SMP product for both the 6 PM ascending and 6 AM descending SMAP overpasses over the first five years of the mission (2015-2020). Consisting of blended precipitation measurements from the GPM (Global Precipitation Mission) satellite constellation, IMERG is treated as the "truth" when comparing to the GEOS model forecasts of precipitation used by SMAP. Key results include: *i)* IMERG measurements generally show higher spatial variability than the GEOS forecast precipitation, *ii)* the IMERG product has a higher frequency of light precipitation amounts, and *iii)* the effect of incorporating IMERG rainfall measurements in lieu of GEOS precipitation forecasts are minimal on the L2SMP retrieval accuracy (determined vs. *in situ* soil moisture measurements at core validation sites). Our results indicate that L2SMP retrievals continue to meet the mission's accuracy requirement (standard deviation of the ubRMSE less than 0.04 m^3/m^3).

Key words: IMERG-precipitationCal, SMAP, GPM, GEOS, soil moisture, precipitation

1. INTRODUCTION

Soil moisture is a critical state variable that controls the land surface water and energy fluxes [Seneviratne et al., 2010, Koster et al., 2004]. There are many applications of remotely sensed soil moisture measurements, including alerting farmers to crop stress, indicating saturated areas where rainfall could trigger landslides, early warning signs of impending droughts, and emergence of dust storms. The National Aeronautics and Space Administration's (NASA) Soil Moisture Active Passive (SMAP) satellite mission [Entekhabi et al., 2014], which launched on 31 January 2015, is the second mission available to monitor global soil moisture along with the European Space Agency's Soil Moisture and Ocean Salinity (SMOS) satellite [Kerr et al., 2012]. SMAP's microwave radiometer operates at an L-band frequency of 1.41 GHz to measure near-surface soil moisture (~ 5 cm topsoil) with a global revisit of 2–3 days. Soil moisture retrievals from passive microwave measurements have been extensively studied during the past ~30 years [Jackson et al., 1999; Jackson and Schmugge, 1991; Mo et al., 1982; Schmugge and Choudhury, 1981], utilizing both model simulations and measurements from field campaigns using truck-based, airborne, and satellite radiometers. Calibration and validation efforts to improve SMAP soil moisture retrieval accuracy (accuracy target = 0.04 m^3/m^3) continue to occur through dedicated field campaigns, analyses of data from both core sites and spatially distributed *in situ* stations [Chan et al., 2016; Colliander et al., 2017; McNairn et al., 2014], global models and comparisons with soil moisture products from SMOS mission.

The SMAP standard Level-2 (L2) passive soil moisture product (L2SMP) contains radiometer-derived soil moisture, brightness temperatures, geolocation, ancillary data, and quality-assessment flags. The SMAP Single Channel Algorithm-V-pol (SCA-V) baseline algorithm (and two other option algorithms: Single Channel Algorithm-H-pol (SCA-H), Dual Channel Algorithm

(DCA)) are used to retrieve soil moisture if all of the input, ancillary, and land surface condition data meet the retrievability criteria. The sensitivity of brightness temperature to ancillary data such as vegetation water content (VWC), surface roughness, surface temperature etc., and their impact on soil moisture retrieval accuracy are examined in past works [Du et al., 2000; Ferrazzoli et al., 1992; Flores et al., 2009; Neelam et al., 2020; Neelam and Mohanty, 2015; Ulaby et al., 1983; Wigneron et al., 2017]. However, there have been no studies (at the time of this analysis) using either real-time observations or model simulations to evaluate the impact of heavy precipitation on SMAP measurements. A large precipitation event can cause short-term surface wetting of vegetation and/or ponding of water on the soil surface which affects the radiometer's sensing depth due to changes in the dielectric constant of the scene. Therefore, it is desirable to flag any SMAP observations and retrievals based on ancillary knowledge of recent precipitation at a given location to avoid overestimation of soil moisture. Since SMAP does not have the ability to detect rain by an independent means, it relies on outside ancillary data sources.

Currently, SMAP's L2SMP soil moisture algorithm includes flagging which indicates the presence or absence of precipitation at the time of a SMAP overpass based on 3 hr time-average precipitation estimates from the Goddard Earth Observing System (GEOS) Forward Processing (FP) numerical weather prediction system (https://gmao.gsfc.nasa.gov/GMAO_products). The algorithm considers a heavy precipitation event to have occurred if the forecast precipitation rate $\boldsymbol{P} \geq 1\text{mm h}^{-1}$. This threshold is the pre-launch criteria selected for the SMAP mission based on the understanding that $\boldsymbol{P} \geq 1\text{mm h}^{-1}$ may result in higher non-uniform soil moisture profile and/or surface ponding, and soil moisture retrieval under such circumstances should be used/interpreted with caution due to potentially inaccurate soil moisture retrieval. In addition to this, it is impossible to determine the exact timing of the precipitation event during SMAP overpass from 3 hr GEOS-

FP precipitation forecasts. For example, soil moisture profile might vary for the precipitation event which occurred 2 mins before the SMAP overpass versus an event which occurred 3 hr before the SMAP overpass. Also, apart from precipitation threshold, the surface ponding also depends on prior factors such as soil moisture conditions, soil texture, soil compaction etc. For example, a rain event on dry soils allow water to move quickly through pores and cracks than wet soils. This movement is further influenced by soil texture i.e., water moves faster through sandy soils due to large pore sizes than it does through small pores of clayey soil. Nonetheless, the current SMAP retrieval algorithm does not use any ancillary estimates of prior soil moisture conditions, and therefore is considered as a scope for future improvements in the algorithm.

The SMAP mission had a choice early in the prelaunch days whether to base SMAP precipitation flagging based on numerical weather model forecasts or use collocated data from other spaceborne instruments capable of detecting rainfall. From a mission risk standpoint prelaunch, SMAP decided to use GEOS precipitation forecasts internal to SMAP and not rely on an external ancillary data source like Global Precipitation Mission (GPM). This decision is reexamined to understand if using GPM IMERG would have produced different soil moisture retrievals (number and quality of soil moisture retrievals) than we currently get using GEOS. The use of an alternate data impacts the SMAP in two different ways: *1)* The GEOS data might miss the precipitation events that might be observed by IMERG. This "misdetection" would result in higher error in soil moisture retrievals; *2)* The GEOS data might indicate precipitation when none was occurring. This "false alarm" would result in data loss though it would not directly impact the SMAP soil moisture assessment statistics.

Precipitation estimates from numerical weather prediction (NWP) models are only as good as the physical models and assimilated data inputs [Accadia et al., 2003; Charba et al., 2003; Dai, 2006]. Uncertainties in the global circulation models (GCMs) "moist physics" algorithms that use 3-dimensional modeling of atmospheric dynamics such as temperature, pressure, humidity, and winds to determine precipitation, land surface models (LSMs), and initial soil moisture distribution have a major impact on the evolution of thermodynamic variables in the planetary boundary layer and subsequently on the precipitation forecasts [Koster, 2004; Koster and Suarez, 1995; Case et al., 2011, Chen and Avissar, 1994,Ookouchi et al., 1984]. The precipitation measurements from *in situ* networks such as rain gauges (although provide direct measurements), are prone to errors such as under-catch caused due to wind effects [Peterson et al., 1998]. In case of weather radars, backscatter radiation is dependent upon the drop size distribution which varies considerably influencing number of rain events detected. The inadequate spatial coverage and representativeness of rain gauge/radar networks are a major drawback to monitor and quantify precipitation on a global basis [Kidd and Huffman, 2011].

On the other hand, satellite-derived precipitation observations serve as an alternative to NWP estimates [Sun et al., 2018] and offer an unparallel advantage to observe precipitation on a global scale. Therefore, frequent, and regular measurements provided by satellites are essential to satisfy the needs of the user community, even though there may be some concerns about the accuracy of the measurements. The near-real time precipitation observations from the GPM satellite mission provides an opportunity for direct grid-to-grid global comparison with GEOS model precipitation estimates. The successful 17-year operational life of the Tropical Rainfall Measuring Mission (TRMM) produced significant improvements in satellite rainfall monitoring [Huffman et al., 2007a]. As a follow-up to TRMM, the GPM Core Observatory (GPM-CO) satellite was launched in February 2014 [Hou et al., 2014; Skofronick-Jackson et al., 2017]. The GPM-CO is a key part of the GPM mission and is designed to be the calibration reference standard for unifying the data from a constellation of passive microwave (PMW) and infrared (IR) satellite platforms. The precipitation estimates are merged through the ***I***ntegrated ***M***ulti-satellit***E*** ***R***etrievals for ***G***PM (IMERG) system [Huffman et al., 2019] to provide PMW-only, IR-only, and merged precipitationCal rainfall products for different latency periods (IMERG–Early ~4 h; IMERG–Late ~14 h; IMERG–Final ~3.5 months).

Therefore**,** in continuation of ongoing efforts to improve the SMAP retrievals, this paper describes the impact of precipitation flagging error on SMAP passive soil moisture retrievals. The main objective of this study is to investigate the impact of GEOS-based precipitation forecasts on the performance of SMAP L2SMP soil moisture retrievals using satellite precipitation observations from GPM. As mentioned earlier, the current SMAP L2SMP algorithm uses GEOS precipitation estimates in the retrieval process to flag the areas with coincident precipitation observations. Since GEOS precipitation estimates have their own errors that can impact the performance of the SMAP L2SMP soil moisture retrievals, we wanted to evaluate the assessment when IMERG is used as an alternate precipitation source. The paper is organized as follows: following this introduction, Section 2 further introduces the L2SMP algorithm, the IMERG-precipitationCal and GEOS-FP precipitation products, and the SMAP Core Validation Site (CVS) data. Section 3 describes the methodologies adopted for this analysis. Results are detailed in Section 4 in terms of performance metrics, statistical evaluation, and analysis of example events. Section 5 contains concluding remarks and plans for future studies.

2. METHODS AND MATERIALS

2.1. SMAP Level 2 Soil Moisture Algorithm

The Level 2 SMAP passive soil moisture product (L2SMP, Version 6.5), derived using SMAP L-band radiometer time-ordered observations (L1B_TB product), are provided on the 36-km global cylindrical Equal-Area Scalable Earth Grid 2.0 (a.k.a. EASE-Grid 2.0), and can be freely downloaded from the National Snow and Ice Data Center (NSIDC) (https://nsidc.org/data/SPL2SMP). The retrieval of soil moisture from SMAP brightness temperature (T_B) observations under vegetation is based on an approximation of the non-linear radiative transfer equation, known as tau-omega model [Mo et al., 1982]:

$$T_{B(p,f,\theta)} = e_{p,f,\theta}.T_{eff}.\Upsilon_{p,f,\theta} + T_c.\left(1-\omega_{p,f,\theta}\right).\left(1-\Upsilon_{p,f,\theta}\right) +$$

$$T_c.\Upsilon_{p,f,\theta}.\left(1-\omega_{p,f,\theta}\right)\left(1-\Upsilon_{p,f,\theta}\right).r_{p,f,\theta} \qquad (1)$$

$$\Upsilon_{p,f,\theta} = \exp\left(-\frac{\tau_{p,f}}{\cos\theta}\right) \qquad (2)$$

where $T_{B(p,f,\theta)}$ is the brightness temperature [K]; T_{eff} is the effective surface temperature [K]; T_c is the effective vegetation temperature [K]; $e_{p,\theta,f}$ is the emissivity of the (rough) soil surface; $r_{p,f,\theta}$ is the rough surface reflectivity; $\tau_{p,f}$ is the nadir optical depth; $\omega_{p,f,\theta}$ is the single scattering albedo. And *p*, θ and *f* denote polarization, look angle and frequency, respectively. This study considers V-polarization only, with constant look angle of 40º at 1.4 GHz frequency. The radiative transfer (equation 1) is essentially approximated as a summation of three components: *1)* the direct emission by soil and one-way attenuation by canopy (the first term), *2)* direct upward emission by canopies (the second term), and *3)* emission by plants and reflected by soil and thereafter attenuated by vegetation (the third term).

The ancillary data used in the soil moisture retrieval process comes from various sources. For example, soil temperatures are provided by the Goddard Earth Observing System (GEOS) model. The optical thickness is estimated as a product of vegetation water content (VWC) and a coefficient (*b*) that characterizes the structure of the canopy. The vegetation water content is estimated using a Normalized Difference Vegetation Index (NDVI) climatology derived from Moderate Resolution Imaging Spectroradiometer (MODIS) data [Jackson et al., 2004]. A more detailed discussion about soil moisture retrieval using the tau-omega model can be found in O'Neill et al., 2019. In SMAP L2SMP algorithm, a binary flag is used to provide information on the retrieval quality and land surface conditions. The surface flag is a 16-bit integer field whose binary representation consists of bits that indicate the presence or absence of certain surface conditions at a grid cell that affects soil moisture retrieval. A summary of surface conditions, flags and their thresholds used in operational production can be found in the SMAP L2SMP ATBD [O'Neill et al., 2019]. Among other surface condition indicators (dense vegetation, mountainous terrain, urban region, etc.,), a flag for the presence or absence of heavy precipitation at the time of the SMAP overpass is provided. The SMAP precipitation flag is the 5th bit in the 16-bit surface quality flag to indicate the surface condition upon the occurrence of precipitation. The flag is developed based on 3 hr precipitation rates from the GEOS FP system (Version 5.13.0 through 5.17) (Section 3, describes precipitation flagging). The evaluation of precipitation flags estimated over 6 hr, 12 hr and 24 hr accumulation periods are also conducted for the five-year period investigated here.

2.2. IMERG precipitationCal

The IMERG Version 06 (V06) level 3 products at 0.1° × 0.1° (~ 11 km) spatial resolution and 30-minute temporal resolution are used in this study. A detailed description of the algorithm and data can be found in Huffman et al. (2019). IMERG is a multi-satellite gridded precipitation product that unifies precipitation estimates from a network of sensors in the GPM constellation. It uses the GPM Core Observatory satellite and as many satellites of opportunity as possible in a very flexible network. The Core Observatory carries the first spaceborne Ku-/Ka-band dual-frequency precipitation radar (DPR) and the multichannel GPM microwave imager (GMI). The GMI instrument (frequency from 10 GHz to 183 GHz) is a 13-channel passive microwave imager. The Combined Radar-Radiometer Algorithm (CORRA) [Olson and Masunaga, 2011] uses data from GMI and DPR [CORRA, Huffman et al., 2007], and calibrates against the Global Precipitation Climatology Project monthly Satellite-Gauge product [Adler et al., 2012]. The Lagrangian time interpolation scheme is applied to the merged constellation estimates using the cloud motion vectors to produce gridded estimates of rainfall. This process is called morphing and was first developed for the Climate Prediction Center Morphing (CMORPH) precipitation estimation algorithm [Joyce et al., 2004; Joyce and Xie, 2011]. When PMW observations are sparse, calibrated IR precipitation estimates are computed using an artificial neural network system, the Precipitation Estimation from Remotely Sensed Information using Artificial Neural Networks-Cloud Classification System (PERSIANN-CCS) algorithm [Hong et al., 2004; Sorooshian et al., 2000]. The PMW observations which are heavily affected by the presence of ice, in such cases IMERG is estimated, *i)* PMW observations are masked out over snowy/icy surfaces, so these regions only have PMW-adjusted IR-based estimates, *ii)* the PMW adjustment to the IR depends on adjustments interpolated from surrounding areas to the areas where PMW observations have been screened out due to snowy/icy surfaces [Huffman, 2019]. IMERG algorithm utilizes a combination of PERSIANN, CMORPH, and CORRA algorithms. It is worth mentioning that PERSIANN estimates the precipitation based on infrared brightness temperature image (as input) and artificial neural network (as a model), while CMORPH is mainly based on microwave data and only uses infrared data when microwave data are not available. The IR precipitation estimates are at higher temporal resolutions, but the accuracy of IR-based estimates is poor due to the indirect relationship between precipitation and IR observations (such as cloud temperature). The PMW precipitation estimates are observed at lower temporal resolutions but are more accurate due to direct association of radiative signatures with precipitation characteristics. The IMERG system runs twice in near-real time (NRT) to accommodate different user requirements for latency and accuracy. The IMERG-Early data are available with 4 hr latency (from the time of observation), where only forward morphing is used, targeting applications such as potential flood or landslide warnings. The IMERG-Late data are available with approximately 14-h latency, where the forward and backward morphing are used, targeting applications such as agricultural forecasting. The IMERG-Final data set is available approximately 3.5 months after the observations and is used for research applications. The IMERG-Final precipitationCal product is calibrated through the Global Precipitation Climatology Centre (GPCC) monthly precipitation gauge data infused via the TMPA approach [Huffman et al., 2007b]. Thus, the IMERG-Final estimates are more accurate and reliable than the Early and Late products [Huffman et al., 2019]. However, to meet the latency requirement for SMAP (less than 24 hrs of acquisition), the IMERG-Early product is used here. For the sake of brevity, the IMERG precipitationCal product is hereafter referred to as IMERG.

2.3. GEOS

The GEOS precipitation data provided to the SMAP project are at 3 hr temporal and 0.25-degree (latitude) by 0.3125-degree (longitude) spatial resolution. The GEOS Forward Processing (FP) system is a global atmospheric data assimilation system [Rienecker, et al., 2008]. It uses an Atmospheric General Circulation Model (AGCM) with primary focus on 3-dimensional modeling of atmospheric dynamics such as temperature, pressure, humidity, and winds. As a part of modeling, the GEOS-FP system assimilates conventional observations and satellite radiances related to temperature, humidity and winds, among other variables [Lucchesi, 2018]. The SMAP L2SMP system regrids the GEOS data to the 36-km EASE2 grid [Brodzik et al., 2012](SMAP Ancillary Data Report: Precipitation. https://smap.jpl.nasa.gov/documents/). Both the GEOS and IMERG precipitation products have global coverage. Since they use different sets of algorithms, parameterizations, and assumptions, a systematic bias between the two products exists. Generally, the "raw" model precipitation from atmospheric analysis systems have significant biases, i.e., the statistical properties of model output may differ from those of the observations [e.g., Vrac and Friederichs, 2014; Case et al., 2011; Adler et al., 2012; Pyle and Brill, 2018]. That is, the model precipitation may be either too high or low, or incorrectly simulate the monsoon (i.e., rainfall starts too early or too late), or overestimate the number of rainfall days and/or underestimate precipitation extremes.

2.4. SMAP Core Validation Sites

The L2SMP soil moisture at 36 km is primarily validated using ground-based *in situ* observations obtained from core validation site (CVS) [Chan et al., 2018], which provide *in situ* soil moisture measurements for locally dense sensor networks. That is, each CVS includes multiple *in situ* soil moisture stations which are matched up in space and time with the corresponding SMAP L2SMP resolution grid [Colliander et al., 2017]. These measurements are spatially aggregated using site-specific and well-established upscaling and calibration functions such that the aggregated soil moisture estimates are representative of the spatial average soil moisture conditions across the EASE-Grid 2.0 grid cell in which the CVS is located [Colliander et al., 2017]. This *in situ* average soil moisture can then be compared to SMAP L2SMP soil moisture retrievals during the validation process [Chan et al., 2018]. Each of these sites is selected such that they cover different geographical locations, climate regimes, and land cover types. The *in situ* data used for the analysis are checked for quality control (QC), where any sudden spikes, drops, missing data etc., are removed before determining the upscaled soil moisture value for each grid cell [O'Neill et al., 2019]. Of 15 CVS's located globally, 13 sites are used in this analysis with measurements taken between April 1, 2015 and March 31, 2020. The remaining two sites (Twente and HOBE) are dropped due to failure to satisfy retrieval quality flags (proximity to water body and urban region). In spite of the dense sensor networks at CVS, we acknowledge that the spatial discrepancy between satellite retrieved and *in situ* soil moisture may introduce uncertainties in soil moisture validation.

3. Methodology

The IMERG half-hourly precipitation estimates originally at 0.1° × 0.1° resolution are converted to 36 km × 36 km EASE-2 grid spatial resolution. A binary (0 and 1) mask is applied while interpolating IMERG to avoid any extrapolation due to no observations. The quality of IMERG and GEOS precipitation data is first assessed using rain gauge data from USDA Agricultural Research Service (ARS) sites [Bosch et al., 2007; Coopersmith et al., 2015; Hanson, 2001; Moran et al., 2008; Steiner et al., 2014]. After assessing the quality of IMERG and GEOS data, the GEOS-based precipitation flag was evaluated against the IMERG-based precipitation flag both globally and during SMAP ascending and descending overpasses using skill scores and performance statistics. This analysis is restricted to 60° N – 60° S, the region within which IMERG provides a consistent coverage. The grid cells representing ocean, large inland water bodies, coastlines, and glaciated surfaces (e.g., Greenland) are excluded from the analysis. An EASE-Grid 2.0 Land-Ocean-Coastline-Ice mask derived from MODIS MOD12Q1 V004 1 km land cover product is used for masking [Friedl et al. 2002]**.** MOD12Q1 utilizes the 17 International Geosphere

Biosphere Programme [IGBP, Belward, 1996] land cover classes. For each grid cell, the percent land is calculated by summing the percent of IGBP non-water classes (1-16). The grid cells >= 50% ice are classified as ice, while cells with >= 50% land and < 50% ice are classified as land, and any remaining cells are classified as ocean (including lakes and inland water).

The skill scores which are frequently used in the precipitation community to verify the accuracy of precipitation estimates over reference data are used for evaluation [Accadia et al., 2003; Charba et al., 2003; Gerrity, 1992; Pyle and Brill, 2018]. The skill scores are obtained from the four elements of a standard contingency table: the number of hits $\boldsymbol{H}$ (GEOS = Yes Rain; IMERG = Yes Rain), misses $\boldsymbol{M}$ (GEOS = No Rain; IMERG = Yes Rain), false alarms $\boldsymbol{F}$ (GEOS = Yes Rain; IMERG = No Rain), and correct rejections $\boldsymbol{C}$ (GEOS = No Rain; IMERG = No Rain). A rain event is considered to be occurring at a given time step if the precipitation rate $\boldsymbol{P}$ is greater than 1mm h^{-1} and is considered to not be occurring if $\boldsymbol{P}$ is less than or equal to 1mm h^{-1}. The ability of the GEOS precipitation estimates to identify the rain events are calculated using four scores: the probability of detection, the false alarm ratio, the threat score, and the Gilbert skill score. The elements of the contingency table and skill scores are computed for every 3 hr window, which are accumulated to represent seasonal [December to February, March to May, June to August, and September to November] and annual skill. A brief description of the skill scores is given below.

The probability of detection (POD) or hit rate (HR) denotes the fraction of the observed precipitation events correctly estimated (ranges from 0 to 1).

$$\mathrm{POD/HR} = \frac{\mathrm{H}}{\mathrm{H+M}} \tag{3}$$

The false alarm ratio (FAR) represents the fraction of precipitation events that did not occur but were incorrectly estimated as rain (ranges from 0 to 1).

$$\mathrm{FAR} = \frac{\mathrm{F}}{\mathrm{H+F}} \tag{4}$$

The threat score (TS), also known as the critical success index (CSI), measures the fraction of observed and/or estimated events that are correctly predicted ignoring the correct rejections (ranges from 0 to 1).

$$\mathrm{TS} = \mathrm{CSI} = \frac{\mathrm{H}}{\mathrm{H+M+F}} \tag{5}$$

The Gilbert skill score (GSS) measures the fraction of observed and/or estimated events that are correctly predicted, adjusted for the frequency of hits associated with random chance (ranges from -1/3 to 1).

$$\mathrm{GSS} = \frac{\mathrm{H-H_R}}{\mathrm{H+M+F-H_R}}, \text{ where } \mathrm{H_R} = \frac{\mathrm{(H+M)(H+F)}}{\mathrm{H+M+F+C}} \tag{6}$$

where ***H*** = number of hits; ***M*** = number of misses/misdetections; ***F*** = number of false alarms; ***C*** = number of correct rejections; H_R = number of hits with random chance.

Performance metrics such as unbiased root mean square error (ubRMSE), root mean square error (RMSE), bias (B), and correlation coefficient (R) are calculated for SMAP soil moisture retrievals using *in situ* soil moisture from core validation sites [Chan et al., 2018]. The performance statistics are computed for the SMAP retrievals with the originally (GEOS-based) precipitation flag and again when misses/ misdetections (GEOS = No Rain; IMERG = Yes Rain) are removed. This performance assessment is conducted for the five-year period April, 2015 - March, 2020, and separately, for ascending (6 PM) and descending (6 AM) SMAP overpasses. The performance assessment is tested for three algorithms, the Single Channel Algorithm-H-pol (SCA-H), the Single Channel Algorithm-V-pol (SCA-V) and Dual Channel Algorithm (DCA), though only the metrics for the SMAP baseline SCA-V are reported here [O'Neill, et al., 2019]. The basic assumptions of the retrieval algorithm such as uniformity of the temperature profiles [Jackson et al., 2010; Owe et al., 2001] are expected more likely to be satisfied by the descending overpass than the ascending overpass. Moreover, precipitation also has a diurnal cycle and 6 PM local time observations are likely to be more impacted due to convective storms especially in warm and humid climates. For this reason, SMAP soil moisture retrievals are separated for ascending and descending overpasses.

4. RESULTS AND DISCUSSION

The performance evaluation of GEOS and IMERG will be discussed in two sections: *i)* a global spatial and temporal (seasonal) skill score assessment, and *ii)* soil moisture accuracy assessment for SMAP ascending and descending overpasses.

4.1. Global Evaluation of IMERG and GEOS Precipitation

The general distribution of precipitation is similar for IMERG and GEOS (Fig. 1). There are significant differences in details observed both spatially and temporally, with intensity of precipitation greatest by far in GEOS precipitation forecasts than in IMERG measurements. The precipitation areas on the path of Inter-tropical Convergence Zone (ITCZ) varies predictably throughout the year, as ITCZ migrates latitudinally on a seasonal basis, Fig. 1. For example, the west coast of India, and the coast of the Asian Pacific show significant precipitation zones in JJA (NH, summer). A strong precipitation band in the North Pacific and North Atlantic is noticed always, which extends eastward in the SON and DJF. Although ITCZ remains near the equator, it moves farther north or south over land than over the oceans because it is drawn toward areas of the warmest surface temperatures. It moves toward the Southern Hemisphere (SH) from September through February and reverses direction in preparation for Northern Hemisphere (NH) Summer.

This movement is expected due to the differential warming of the hemisphere following the sun. An elaborate discussion on the spatial and temporal variability in the precipitation patterns are discussed in past studies [Adler et al., 2017, 2012; Hou et al., 2014; Huffman et al., 2015, 2007c; Maggioni et al., 2016; Reichle et al., 2017]. Regions with significant precipitation differences (Fig. 1) i.e., Amazonia, central Africa, and Southeast Asia show poor correlation between IMERG and GEOS (Fig. 2), while regions over eastern USA, Europe, and parts of China and Australia show a strong correlation (R>0.8). The correlation between IMERG and GEOS also show a seasonal migration with poor values in DJF (JJA) over NH (SH). The precipitation forecasts from GEOS show higher rainfall estimates especially over tropical regions than the satellite based IMERG precipitation. This overestimation by GEOS compared to IMERG especially over the tropics can be attributed to the large land surface heterogeneity uncertainties in the GCM, LSM and initial soil moisture distribution which impact the planetary boundary layer and hence the precipitation forecasts [Koster, 2004; Koster and Suarez, 1995; Case et al., 2011, Chen and Avissar, 1994; Ookouchi et al., 1984]. Studies by Maggioni et al., 2016; Xu et al., 2017, have also shown that regions with complex terrain and high-elevation regions show poorer rain detection. The percentage of detecting very low rain intensities is higher in IMERG and could potentially be related to the more frequent data collected by the constellation of GPM satellite observations used in estimating the IMERG product. Many uncertainties in IMERG data can mainly be attributed to IR morphing to improve the global coverage, which is based on cloud temperature i.e., cold cloud tops suggest more rain. A relationship between cloud top brightness and temperature is used to indicate precipitation rate. This indirect relationship may introduce uncertainties associated with the height, thickness, and type of cloud, and this relationship is uncertain especially over land regions [Sun et al., 2018].

The impact of ITCZ migration is also noticed on skill scores estimated globally Fig. 3(a). For example, in Fig. 3(b) a higher HR is noticed over Eastern USA and Indian Sub-Continent in NH for JJA, while over Central Amazonia and Australia in SH for DJF. As seen in Fig. 4 and Table 1.II, in NH the HR increased for 3 hr and 6 hr precipitation accumulation periods after which it decreased, and this remains true for all four seasons, while for SH, the HR consistently improved with increase in precipitation accumulation period. The FAR followed a U-curve both in SH and NH, where a higher FAR is noticed at 3 hr and 24 hr accumulation periods, except for winter in NH where it decreased consistently with the precipitation accumulation periods. A trend that is like HR is also observed for TS and GSS. The latitudinal distribution of HR and FAR follow an M-curve (Fig. 5) i.e., lowest (highest) HR (FAR) noticed in the ± 20° latitudinal band, a region with high precipitation frequency and intensity. A clear seasonal difference in the latitudinal distribution of HR/FAR is observed over NH than in SH, where the variability within HR/FAR is more random.

The differences between the IMERG precipitation product and GEOS precipitation forecasts are expected given the variability in physical processes, and assumptions used in the respective algorithm development. IMERG generally observes lower precipitation intensities and higher spatial variability than GEOS. Also, the ability to detect light rainfall events is superior in IMERG than GEOS [Sunilkumar et al., 2019; Xu et al., 2017]. A comparison between IMERG and GEOS is conducted with ARS rain gauges at three SMAP CVS (the only SMAP CVS where rain gauge data are available for this analysis), Table 1.I, where a higher HR is observed for IMERG-ARS compared to GEOS-ARS.

4.2. Accuracy Evaluation for SMAP Ascending and Descending Overpasses

In general, rainfall maxima are reported in the mid- to late afternoon for land regions [Yang and Smith, 2006]. This is because during afternoon/evening time when the land surface is still warm there is a rapid upward convection of hot air which collides with the cool upper air in the atmosphere, resulting in a rain event. A higher HR and lower FAR during afternoon/evening can also be noticed from SMAP ascending overpass than from SMAP descending overpass (morning), Fig. 6. Similarly, the number of correct rejections, i.e., no rain events, are also found to be lower during ascending overpasses, and higher during descending overpasses.

The key results from this analysis, i.e., evaluation of misdetections (section 3) on soil moisture retrieval accuracy are summarized in Table 2 (I and II). Among the three algorithms (SCA-H, SCA-V, DCA), SCA-V shows superior performance and was able to deliver the best overall retrieval results, achieving an average ubRMSE of 0.0362 m^3/m^3 (6 AM descending) and 0.0350 m^3/m^3 (6 PM ascending). With misdetections removed, the ubRMSE slightly improved to 0.0359 m^3/m^3 (6 AM descending) and 0.0347 m^3/m^3 (6 PM ascending). Correlations of 0.811 for 6 AM descending overpass show a marginally increase to 0.812, while for 6 PM ascending overpass the correlation remain same at 0.815 even after misdetections are removed. These results remain true for different precipitation accumulation durations. For SMAP ascending (descending) overpasses, the number of misdetections decreased (increased) with increase in precipitation accumulation periods i.e., 3 hr, 6 hr, 12 hr and 24 hr as shown in Fig. 7(a)-b. This may be because the probability of convective storms which are more likely to occur during SMAP ascending overpasses (6 PM) gets diminished with an increase in the accumulation period. In the case of SMAP descending overpass (6 AM) which typically observe less rain events, the accumulation period increases the probability of rain events. For both SMAP ascending and descending overpasses, the number of misdetections generally decreased with an increase in precipitation threshold i.e., 0.5 mm, 1 mm, 2 mm, and 3 mm (Fig. 7(b)). The number of misdetections is similar for ≤ 1 mm/hr threshold i.e., 0.5 mm/hr and 1 mm/hr and for ≥ 1 mm/hr i.e., 2 mm/hr and 3 mm/hr thresholds, except for few agricultural (temperate) and grasslands (semi-arid) sites such as Remedhus, Reynolds Creek, Little River and Walnut Gulch where sudden highly convective storms are developed during SMAP ascending overpasses. Generally, a consistent decrease in ubRMSE is noticed across all sites Table 2 (I and II). Due to the time, it takes for a wetting front to travel from the soil surface to soil sensors at depth, there may be times that SMAP receives a surface wetness signal before the signal reaches *in situ* soil sensors. Our results also concur with a recent study conducted at field scale by Colliander et al., 2020, using precipitation gauge data to evaluate the impact of precipitation events on SMAP soil moisture. Their results showed, the ubRMSE of soil moisture improved by 0.008 m^3/m^3, while the correlation increase by 0.01 by increasing the length of the precipitation time window from 3 hr to 36 hr. It is also worth mentioning that the analysis was conducted using the IMERG-PMW (microwave-only, section 2.2) product, and a similar effect on retrieval accuracy was observed, although the IMERG-PMW product had spatial gaps in its coverage which changed the number of observations used in the analysis. In the case of bias, an average of 0.0092 m^3/m^3 (6 AM descending) and 0.0118 m^3/m^3 (6 PM ascending), changed to 0.0093 m^3/m^3 (6 AM descending) and 0.0121 m^3/m^3 (6 PM ascending) after accounting for misdetections. An increase in soil moisture bias is expected if SMAP wrongly retrieves soil moisture during a rain event due to the lack of a precipitation forecast from GEOS. If a rain event occurs during a SMAP overpass, SMAP will sense all types of surface wetness such as ponded rainwater on the soil or vegetation surfaces before the wetting front percolates and the wetness signal from the rain event is detected by the *in situ* soil moisture sensors at depth. This potential mismatch at times between the “soil moisture” SMAP retrieves from the wet surface and the typically drier soil moisture measured by *in situ* sensors at ~5 cm depth at the time of the rain event (close to the overpass) can cause biased retrieval. Apart from bias caused due to precipitation events which generally are higher during SMAP ascending overpasses, the differences in the bias for 6 PM ascending and 6 AM descending SMAP overpasses [Chan et al., 2018] can also be attributed to higher uniformity in the vertical temperature profile both in the soil and between the soil and the air and vegetation layer immediately above the soil at 6 AM [O'Neill et al., 2019]. Further refinements in the correction procedure for the effective soil temperature described in [Chan et al., 2016; Choudhury et al., 1982] are expected to improve the observed biases and reduce the small performance gap between the ascending and descending soil moisture estimates.

In spite of the relatively higher performance of IMERG in detecting rain events, there are several reasons to reasonably argue why the skill of the IMERG does not contribute towards improving the retrieval accuracy of SMAP soil moisture or lessening the number of non-retrievals compared to using GEOS precipitation forecasts: *i)* the number of precipitation events (hits + misses) do not significantly change with respect to the total number of observations used in estimating SMAP soil moisture retrieval accuracy when using IMERG compared to GEOS. Because, SMAP has a revisit time of ~2-3 days this reduces the number of rain and no-rain observations. If a rain event occurs outside the overpass window, i.e., either before or after the 3 hr time window used to calculate precipitation flagging, then a no-rain event (correction rejection) is considered; *ii)* the spatial discrepancy between the *in situ* observations, SMAP soil moisture, and spatial aggregation of IMERG. And each of these datasets have their uncertainties/limitations with respect to sparsity in coverage, parameterizations used in land surface models, IR morphing in IMERG, models used in the retrieval algorithm, etc. The combination of these possible factors does not demonstrate a strong case for the use of IMERG precipitation measurements over GEOS precipitation forecasts in setting the precipitation flags used in SMAP soil moisture retrievals.

5. CONCLUSION

The Global Precipitation Mission (GPM) (observation) precipitation data provide a unique opportunity for direct grid-to-grid global comparison with GEOS (model) precipitation estimates to evaluate SMAP precipitation flagging. The assessment has been conducted using the half-hourly merged (microwave and infrared) rainfall estimates from IMERG-E for the period of April 2015 – March 2020. Based on comparison with *in situ* soil moisture observations from CVS, the SMAP 36-km radiometer-based soil moisture (L2SMP) data product continues to perform within the targeted SMAP mission requirements accuracy (0.04 m^3/m^3) with the current specifications for precipitation quality flags based on GEOS precipitation estimates. The ubRMSE of the SMAP soil moisture product improved slightly from 0.0362 m^3/m^3 (6 AM descending) and 0.0350 m^3/m^3 (6 PM ascending) to 0.0359 m^3/m^3 (6 AM descending) and 0.0347 m^3/m^3 (6 PM ascending), because of removing precipitation events as detected from IMERG but not forecast by GEOS. This improvement in performance metrics was not significantly large enough to warrant a switch at the present time from the use of GEOS forecasts to IMERG measurements in setting SMAP precipitation flags. For future work, a synthetic experiment can be performed to understand precipitation flagging and its impact on soil moisture accuracy beyond CVS sites. Nevertheless, the studies using synthetic precipitation dataset should be interpreted cautiously for the uncertainties (model/algorithms and input variables) associated in the process.

Acknowledgments

The research described in this publication was carried out at the National Aeronautics and Space Administration, Goddard Space Flight Center. The work was conducted under funding provided by the SMAP Project and the SMAP Science Team. We appreciate the constructive feedback provided by 3 anonymous reviewers and the editors.

References

Accadia, C., Mariani, S., Casaioli, M., Lavagnini, A., Speranza, A., 2003. Sensitivity of precipitation forecast skill scores to bilinear interpolation and a simple nearest-neighbor average method on high-resolution verification grids. Weather Forecast. 18, 918–932.

Adler, R.F., Gu, G., Huffman, G.J., 2012. Estimating Climatological Bias Errors for the Global Precipitation Climatology Project (GPCP). J. Appl. Meteorol. Climatol. 51, 84–99. https://doi.org/10.1175/JAMC-D-11-052.1

Adler, R.F., Gu, G., Sapiano, M., Wang, J.-J., Huffman, G.J., 2017. Global Precipitation: Means, Variations and Trends During the Satellite Era (1979–2014). Surv. Geophys. 38, 679–699. https://doi.org/10.1007/s10712-017-9416-4

Belward, A., 1996. The IGBP-DIS Global 1km Land Cover Data Set. *Proposal and implementation plans. International Geosphere-Biosphere Program–Data and Information System working paper*, *13*.

Bosch, D.D., Sheridan, J.M., Marshall, L.K., 2007. Precipitation, soil moisture, and climate database, Little River experimental watershed, Georgia, United States. Water Resour. Res. 43.

Brodzik, M.J., Billingsley, B., Haran, T., Raup, B., Savoie, M.H., 2012. EASE-Grid 2.0: Incremental but Significant Improvements for Earth-Gridded Data Sets. ISPRS Int. J. Geo-Inf. 1, 32–45. https://doi.org/10.3390/ijgi1010032

Case, J.L., Kumar, S.V., Srikishen, J., Jedlovec, G.J., 2011. Improving Numerical Weather Predictions of Summertime Precipitation over the Southeastern United States through a High-

Resolution Initialization of the Surface State. Weather Forecast. 26, 785–807. https://doi.org/10.1175/2011WAF2222455.1

Chan, S.K., Bindlish, R., O'Neill, P., Jackson, T., Njoku, E., Dunbar, S., Chaubell, J., Piepmeier, J., Yueh, S., Entekhabi, D., 2018. Development and assessment of the SMAP enhanced passive soil moisture product. Remote Sens. Environ. 204, 931–941.

Chan, S.K., Bindlish, R., O'Neill, P.E., Njoku, E., Jackson, T., Colliander, A., Chen, F., Burgin, M., Dunbar, S., Piepmeier, J., Yueh, S., Entekhabi, D., Cosh, M.H., Caldwell, T., Walker, J., Wu, X., Berg, A., Rowlandson, T., Pacheco, A., McNairn, H., Thibeault, M., Martínez-Fernández, J., González-Zamora, Á., Seyfried, M., Bosch, D., Starks, P., Goodrich, D., Prueger, J., Palecki, M., Small, E.E., Zreda, M., Calvet, J., Crow, W.T., Kerr, Y., 2016. Assessment of the SMAP Passive Soil Moisture Product. IEEE Trans. Geosci. Remote Sens. 54, 4994–5007. https://doi.org/10.1109/TGRS.2016.2561938

Charba, J.P., Reynolds, D.W., McDonald, B.E., Carter, G.M., 2003. Comparative verification of recent quantitative precipitation forecasts in the National Weather Service: A simple approach for scoring forecast accuracy. Weather Forecast. 18, 161–183.

Chen, F., Avissar, R., 1994. The Impact of Land-Surface Wetness Heterogeneity on Mesoscale Heat Fluxes. J. Appl. Meteorol. 33, 1323–1340. https://doi.org/10.1175/1520-0450(1994)033<1323:TIOLSW>2.0.CO;2

Colliander, A., Jackson, T.J., Berg, A., Bosch, D.D., Caldwell, T., Chan, S., Cosh, M.H., Collins, C.H., Martinez-Fernandez, J., McNairn, H., Prueger, J.H., Starks, P.J., Walker, J.P., Yueh, S.H., 2020. Effect of Rainfall Events on SMAP Radiometer-Based Soil Moisture Accuracy Using Core Validation Sites. J. Hydrometeorol. JHM-D-19-0122.1. https://doi.org/10.1175/JHM-D-19-0122.1

Colliander, A., Jackson, T.J., Bindlish, R., Chan, S., Das, N., Kim, S., Cosh, M., Dunbar, R., Dang, L., Pashaian, L., 2017. Validation of SMAP surface soil moisture products with core validation sites. Remote Sens. Environ. 191, 215–231.

Coopersmith, E.J., Cosh, M.H., Petersen, W.A., Prueger, J., Niemeier, J.J., 2015. Soil moisture model calibration and validation: An ARS watershed on the South Fork Iowa River. J. Hydrometeorol. 16, 1087–1101.

Dai, A., 2006. Precipitation Characteristics in Eighteen Coupled Climate Models. J. Clim. 19, 4605–4630. https://doi.org/10.1175/JCLI3884.1

Du, Y., Ulaby, F.T., Dobson, M.C., 2000. Sensitivity to soil moisture by active and passive microwave sensors. IEEE Trans. Geosci. Remote Sens. 38, 105–114. https://doi.org/10.1109/36.823905

Entekhabi, D., Yueh, S., O'Neill, P.E., Kellogg, K.H., Allen, A., Bindlish, R., Brown, M., Chan, S., Colliander, A., Crow, W.T., 2014. SMAP handbook–soil moisture active passive: Mapping soil moisture and freeze/thaw from space.

Ferrazzoli, P., Paloscia, S., Pampaloni, P., Schiavon, G., Solimini, D., Coppo, P., 1992. Sensitivity of microwave measurements to vegetation biomass and soil moisture content: a case study. IEEE Trans. Geosci. Remote Sens. 30, 750–756. https://doi.org/10.1109/36.158869

Flores, A.N., Ivanov, V.Y., Entekhabi, D., Bras, R.L., 2009. Impact of hillslope-scale organization of topography, soil moisture, soil temperature, and vegetation on modeling surface microwave radiation emission. IEEE Trans. Geosci. Remote Sens. 47, 2557–2571.

Friedl, M.A., McIver, D.K., Hodges, J.C., Zhang, X.Y., Muchoney, D., Strahler, A.H., Woodcock, C.E., Gopal, S., Schneider, A., Cooper, A. and Baccini, A., 2002. Global Land Cover Mapping from MODIS: Algorithms and Early Results. Remote Sensing of the Environment 83: 287-302.

Gerrity, J.P., 1992. A Note on Gandin and Murphy's Equitable Skill Score. Mon. Weather Rev. 120, 2709–2712. https://doi.org/10.1175/1520-0493(1992)120<2709:ANOGAM>2.0.CO;2

Hanson, C.L., 2001. Long-term precipitation database, reynolds creek experimental watershed, Idaho, United States. Water Resour. Res. 37, 2831–2834.

Hong, Y., Hsu, K.-L., Sorooshian, S., Gao, X., 2004. Precipitation Estimation from Remotely Sensed Imagery Using an Artificial Neural Network Cloud Classification System. J. Appl. Meteorol. 43, 1834–1853. https://doi.org/10.1175/JAM2173.1

Hou, A.Y., Kakar, R.K., Neeck, S., Azarbarzin, A.A., Kummerow, C.D., Kojima, M., Oki, R., Nakamura, K., Iguchi, T., 2014. The global precipitation measurement mission. Bull. Am. Meteorol. Soc. 95, 701–722.

Huffman, G., 2019. IMERG V06 Quality Index.

Huffman, G.J., Bolvin, D.T., Braithwaite, D., Hsu, K., Joyce, R., Xie, P., Yoo, S.-H., 2015. NASA global precipitation measurement (GPM) integrated multi-satellite retrievals for GPM (IMERG). Algorithm Theor. Basis Doc. Version 4, 30.

Huffman, G.J., Bolvin, D.T., Nelkin, E.J., Wolff, D.B., Adler, R.F., Gu, G., Hong, Y., Bowman, K.P., Stocker, E.F., 2007a. The TRMM Multisatellite Precipitation Analysis (TMPA): Quasi-Global, Multiyear, Combined-Sensor Precipitation Estimates at Fine Scales. J. Hydrometeorol. 8, 38–55. https://doi.org/10.1175/JHM560.1

Huffman, G.J., Bolvin, D.T., Nelkin, E.J., Wolff, D.B., Adler, R.F., Gu, G., Hong, Y., Bowman, K.P., Stocker, E.F., 2007b. The TRMM Multisatellite Precipitation Analysis (TMPA): Quasi-Global, Multiyear, Combined-Sensor Precipitation Estimates at Fine Scales. J. Hydrometeorol. 8, 38–55. https://doi.org/10.1175/JHM560.1

Huffman, G.J., Bolvin, D.T., Nelkin, E.J., Wolff, D.B., Adler, R.F., Gu, G., Hong, Y., Bowman, K.P., Stocker, E.F., 2007c. The TRMM Multisatellite Precipitation Analysis (TMPA): Quasi-Global, Multiyear, Combined-Sensor Precipitation Estimates at Fine Scales. J. Hydrometeorol. 8, 38–55. https://doi.org/10.1175/JHM560.1

Jackson, T.J., Chen, D., Cosh, M., Li, F., Anderson, M., Walthall, C., Doriaswamy, P., Hunt, E.R., 2004. Vegetation water content mapping using Landsat data derived normalized difference water index for corn and soybeans. Remote Sens. Environ. 92, 475–482.

Jackson, T.J., Cosh, M.H., Bindlish, R., Starks, P.J., Bosch, D.D., Seyfried, M., Goodrich, D.C., Moran, M.S., Du, J., 2010. Validation of Advanced Microwave Scanning Radiometer Soil Moisture Products. IEEE Trans. Geosci. Remote Sens. 48, 4256–4272. https://doi.org/10.1109/TGRS.2010.2051035

Jackson, T.J., Le Vine, D.M., Hsu, A.Y., Oldak, A., Starks, P.J., Swift, C.T., Isham, J.D., Haken, M., 1999. Soil moisture mapping at regional scales using microwave radiometry: The Southern Great Plains Hydrology Experiment. IEEE Trans. Geosci. Remote Sens. 37, 2136–2151.

Jackson, T.J., Schmugge, T.J., 1991. Vegetation effects on the microwave emission of soils. Remote Sens. Environ. 36, 203–212.

Joyce, R.J., Janowiak, J.E., Arkin, P.A., Xie, P., 2004. CMORPH: A Method that Produces Global Precipitation Estimates from Passive Microwave and Infrared Data at High Spatial and Temporal Resolution. J. Hydrometeorol. 5, 17.

Joyce, R.J., Xie, P., 2011. Kalman Filter–Based CMORPH. J. Hydrometeorol. 12, 1547–1563. https://doi.org/10.1175/JHM-D-11-022.1

Kerr, Y.H., Waldteufel, P., Richaume, P., Wigneron, J.P., Ferrazzoli, P., Mahmoodi, A., Al Bitar, A., Cabot, F., Gruhier, C., Juglea, S.E., 2012. The SMOS soil moisture retrieval algorithm. IEEE Trans. Geosci. Remote Sens. 50, 1384–1403.

Kidd, C., and Huffman, G., 2011. Global precipitation measurement. *Meteorological Applications*, *18*(3), 334-353.

Kidd, C., Becker, A., Huffman, G.J., Muller, C.L., Joe, P., Skofronick-Jackson, G., Kirschbaum, D.B., 2017. So, How Much of the Earth's Surface *Is* Covered by Rain Gauges? Bull. Am. Meteorol. Soc. 98, 69–78. https://doi.org/10.1175/BAMS-D-14-00283.1

Koster, R.D., Dirmeyer, P.A., Guo, Z., Bonan, G., Chan, E., Cox, P., Gordon, C.T., Kanae, S., Kowalczyk, E., Lawrence, D. and Liu, P., 2004. Regions of strong coupling between soil moisture and precipitation. *Science*, *305*(5687), pp.1138-1140.

Koster, R.D., 2004. Regions of Strong Coupling Between Soil Moisture and Precipitation. Science 305, 1138–1140. https://doi.org/10.1126/science.1100217

Koster, R.D., Suarez, M.J., 1995. Relative contributions of land and ocean processes to precipitation variability. J. Geophys. Res. Atmospheres 100, 13775–13790. https://doi.org/10.1029/95JD00176

Lucchesi, R., 2013. File Specification for GEOS-5 FP-IT (Forward Processing for Instrument Teams).

Maggioni, V., Meyers, P.C., Robinson, M.D., 2016. A Review of Merged High-Resolution Satellite Precipitation Product Accuracy during the Tropical Rainfall Measuring Mission (TRMM) Era. J. Hydrometeorol. 17, 17.

McNairn, H., Jackson, T.J., Wiseman, G., Belair, S., Berg, A., Bullock, P., Colliander, A., Cosh, M.H., Kim, S.-B., Magagi, R., 2014. The soil moisture active passive validation experiment 2012 (SMAPVEX12): Prelaunch calibration and validation of the SMAP soil moisture algorithms. IEEE Trans. Geosci. Remote Sens. 53, 2784–2801.

M.M. Rienecker, M.J. Suarez, R. Todling, J. Bacmeister, L. Takacs, H.-C. Liu, W. Gu, M. Sienkiewicz,R.D. Koster, R. Gelaro, I. Stajner, and J.E. Nielsen, 2008. The GEOS-5 Data Assimilation System— Documentation of Versions 5.0.1, 5.1.0, and 5.2.0 [WWW Document]. URL https://gmao.gsfc.nasa.gov/pubs/docs/Rienecker369.pdf (accessed 7.9.20).

Mo, T., Choudhury, B.J., Schmugge, T.J., Wang, J.R., Jackson, T.J., 1982. A model for microwave emission from vegetation-covered fields. J. Geophys. Res. Oceans 87, 11229–11237.

Moran, M.S., Holifield Collins, C.D., Goodrich, D.C., Qi, J., Shannon, D.T., Olsson, A., 2008. Long-term remote sensing database, Walnut Gulch Experimental Watershed, Arizona, United States. Water Resour. Res. 44.

Neelam, M., Colliander, A., Mohanty, B.P., Cosh, M.H., Misra, S., Jackson, T.J., 2020. Multiscale Surface Roughness for Improved Soil Moisture Estimation. IEEE Trans. Geosci. Remote Sens. 1–13. https://doi.org/10.1109/TGRS.2019.2961008

Neelam, M., Mohanty, B.P., 2015. Global sensitivity analysis of the radiative transfer model. Water Resour. Res. 51, 2428–2443.

Olson, W.S., Masunaga, H., n.d. GPM Combined Radar-Radiometer Precipitation Algorithm Theoretical Basis Document (Version 4) 63.

O'Neill, P.E., Njoku, E.G., Jackson, T.J., Chan, S., Bindlish, R., 2019. SMAP algorithm theoretical basis document: Level 2 & 3 soil moisture (passive) data products. Jet Propuls. Lab Calif. Inst Technol Pasadena CA USA JPL -66480.

Ookouchi, Y., Segal, M., Kessler, R.C., Pielke, R.A., 1984. Evaluation of Soil Moisture Effects on the Generation and Modification of Mesoscale Circulations. Mon. Weather Rev. 112, 2281–2292. https://doi.org/10.1175/1520-0493(1984)112<2281:EOSMEO>2.0.CO;2

Owe, M., de Jeu, R., Walker, J., 2001. A methodology for surface soil moisture and vegetation optical depth retrieval using the microwave polarization difference index. IEEE Trans. Geosci. Remote Sens. 39, 1643–1654. https://doi.org/10.1109/36.942542

Peterson, T.C., Easterling, D.R., Karl, T.R., Groisman, P., Nicholls, N., Plummer, N., Torok, S., Auer, I., Boehm, R., Gullett, D. and Vincent, L., 1998. Homogeneity adjustments of in situ atmospheric climate data: a review. *International Journal of Climatology: A Journal of the Royal Meteorological Society*, *18*(13), pp.1493-1517.

Pyle, M.E., Brill, K.F., 2018. A Comparison of Two Methods for Bias Correcting Precipitation Skill Scores. Weather Forecast. 34, 3–13. https://doi.org/10.1175/WAF-D-18-0109.1

Reichle, R.H., Liu, Q., Koster, R.D., Draper, C.S., Mahanama, S.P.P., Partyka, G.S., 2017. Land Surface Precipitation in MERRA-2. J. Clim. 30, 22.

Schmugge, T.J., Choudhury, B.J., 1981. A comparison of radiative transfer models for predicting the microwave emission from soils. Radio Sci. 16, 927–938.

Seneviratne, S.I., Corti, T., Davin, E.L., Hirschi, M., Jaeger, E.B., Lehner, I., Orlowsky, B. and Teuling, A.J., 2010. Investigating soil moisture–climate interactions in a changing climate: A review. *Earth-Science Reviews*, *99*(3-4), pp.125-161.

Skofronick-Jackson, G., Petersen, W.A., Berg, W., Kidd, C., Stocker, E.F., Kirschbaum, D.B., Kakar, R., Braun, S.A., Huffman, G.J., Iguchi, T., Kirstetter, P.E., Kummerow, C., Meneghini, R., Oki, R., Olson, W.S., Takayabu, Y.N., Furukawa, K., Wilheit, T., 2017. The Global Precipitation Measurement (GPM) Mission for Science and Society. Bull. Am. Meteorol. Soc. 98, 1679–1695. https://doi.org/10.1175/BAMS-D-15-00306.1

Sorooshian, S., Hsu, K.-L., Gao, X., Gupta, H.V., Imam, B., Braithwaite, D., 2000. Evaluation of PERSIANN system satellite-based estimates of tropical rainfall. Bull. Am. Meteorol. Soc. 81, 2035–2046.

Steiner, J.L., Starks, P.J., Garbrecht, J.D., Moriasi, D.N., Zhang, X., Schneider, J.M., Guzman, J.A., Osei, E., 2014. Long-Term Environmental Research: The Upper Washita River Experimental Watersheds, Oklahoma, USA. J. Environ. Qual. 43, 1227–1238.

Sun, Q., Miao, C., Duan, Q., Ashouri, H., Sorooshian, S., Hsu, K.-L., 2018. A Review of Global Precipitation Data Sets: Data Sources, Estimation, and Intercomparisons. Rev. Geophys. 56, 79–107. https://doi.org/10.1002/2017RG000574

Ulaby, F.T., Razani, M., Dobson, M.C., 1983. Effects of Vegetation Cover on the Microwave Radiometric Sensitivity to Soil Moisture. IEEE Trans. Geosci. Remote Sens. GE-21, 51–61. https://doi.org/10.1109/TGRS.1983.350530

Vrac, M., Friederichs, P., 2014. Multivariate—Intervariable, Spatial, and Temporal—Bias Correction. J. Clim. 28, 218–237. https://doi.org/10.1175/JCLI-D-14-00059.1

Wigneron, J.-P., Jackson, T.J., O'Neill, P., De Lannoy, G., De Rosnay, P., Walker, J.P., Ferrazzoli, P., Mironov, V., Bircher, S., Grant, J.P., 2017. Modelling the passive microwave signature from land surfaces: A review of recent results and application to the L-band SMOS & SMAP soil moisture retrieval algorithms. Remote Sens. Environ. 192, 238–262.

Xu, R., Tian, F., Yang, L., Hu, H., Lu, H., Hou, A., 2017. Ground validation of GPM IMERG and TRMM 3B42V7 rainfall products over southern Tibetan Plateau based on a high-density rain gauge network. J. Geophys. Res. Atmospheres 122, 910–924. https://doi.org/10.1002/2016JD025418

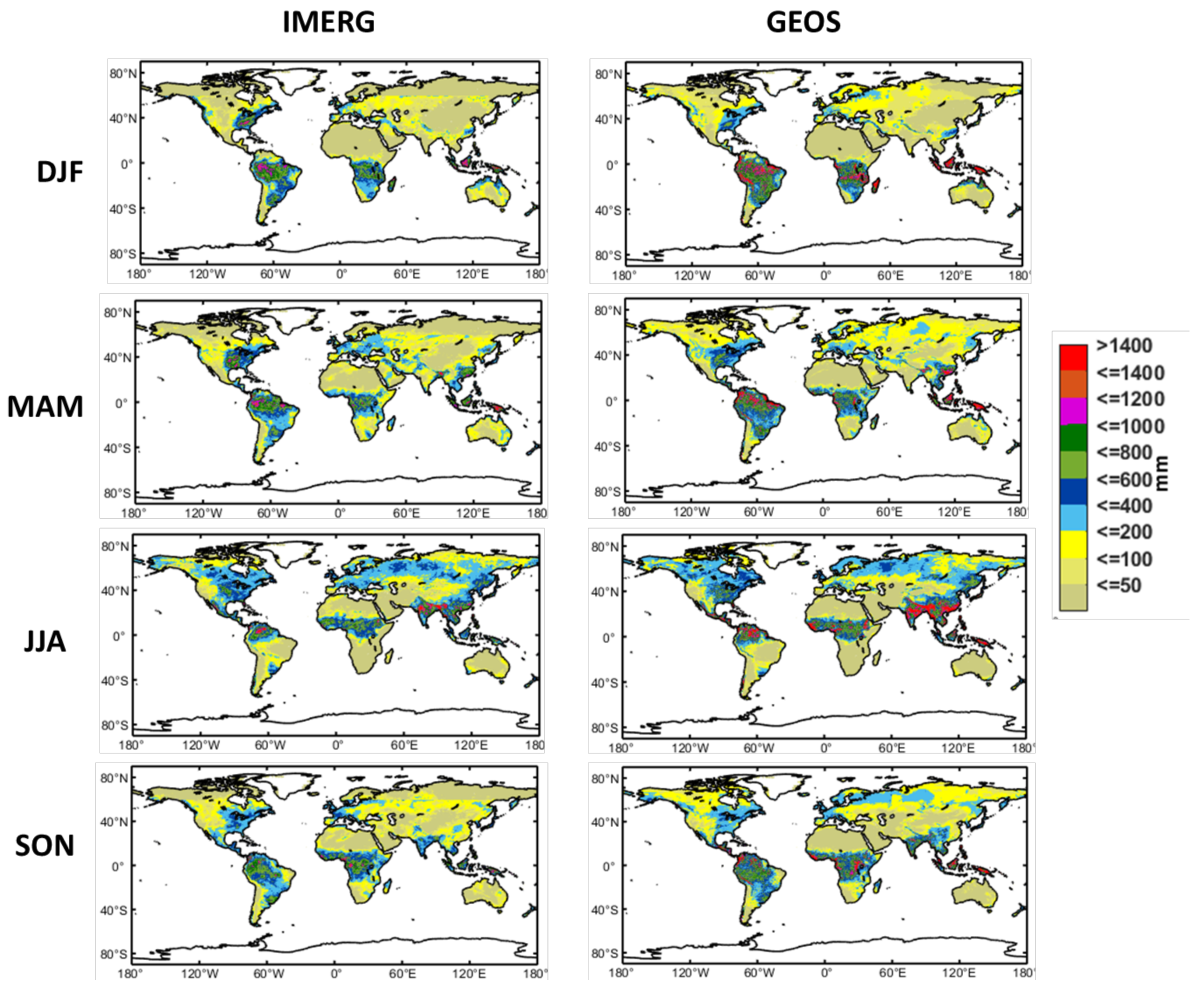

Figure 1: The seasonal [DJF, MAM, JJA, and SON] precipitation accumulation for IMERG (left) and GEOS (right), 2019.

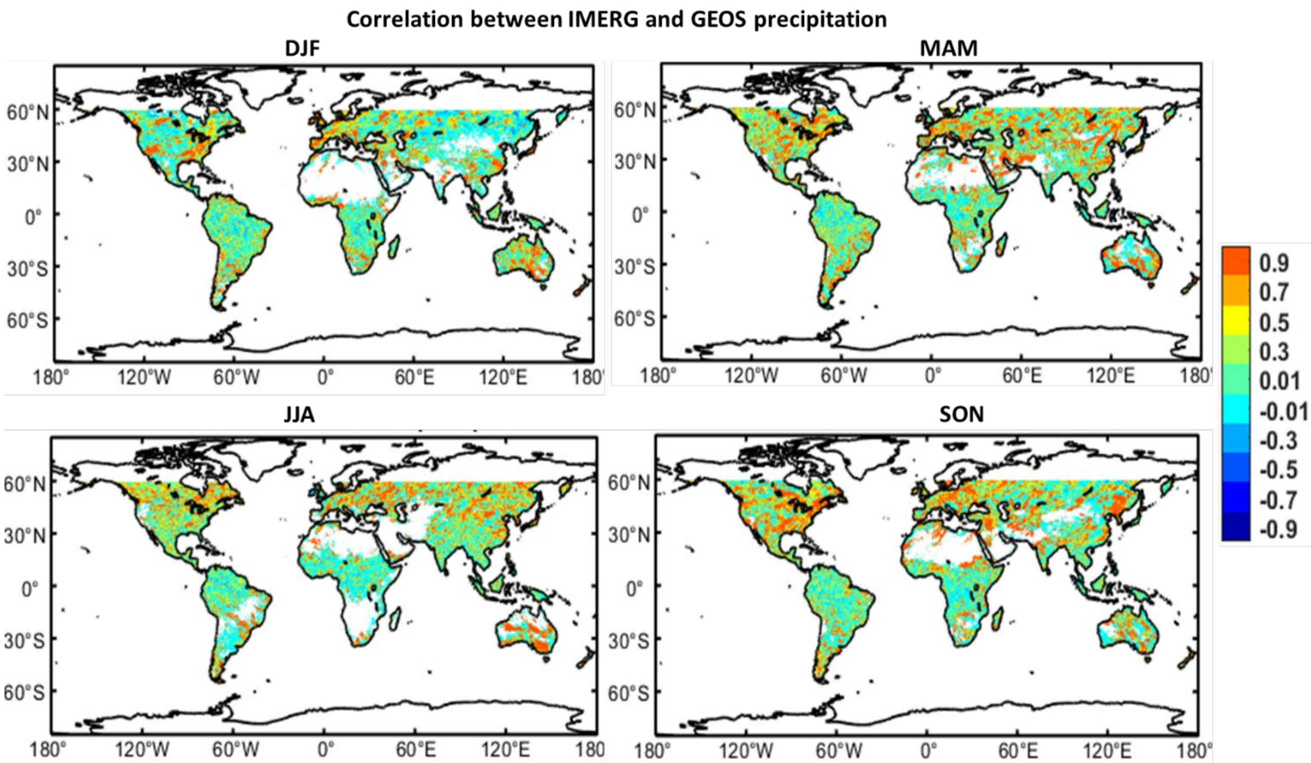

Figure 2: The seasonal variability in correlation between IMERG and GEOS precipitation products estimated from April 2015 – March 2020.

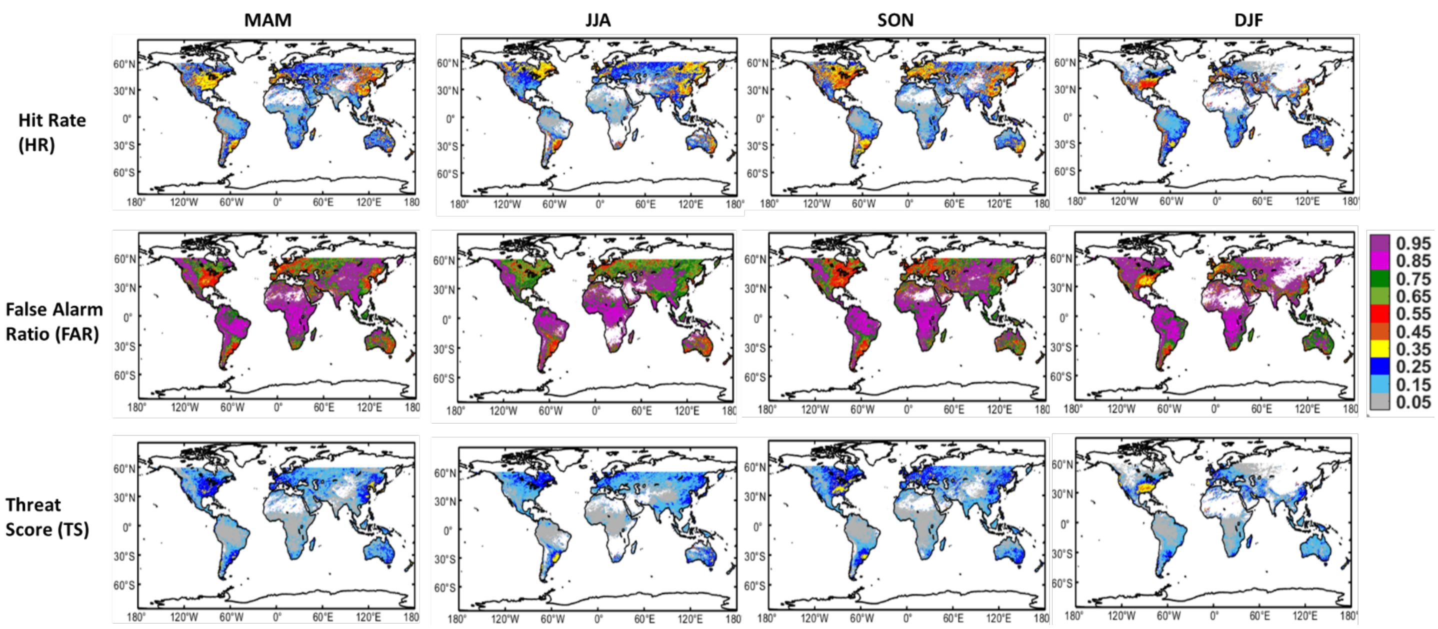

Figure 3(a): Global variations in skill scores estimation from April, 2015-March, 2020: I) Hit Rate (HR), II) False Alarm Ratio (FAR), III) Threat Score (TS) over DJF, MAM, JJA and SON.

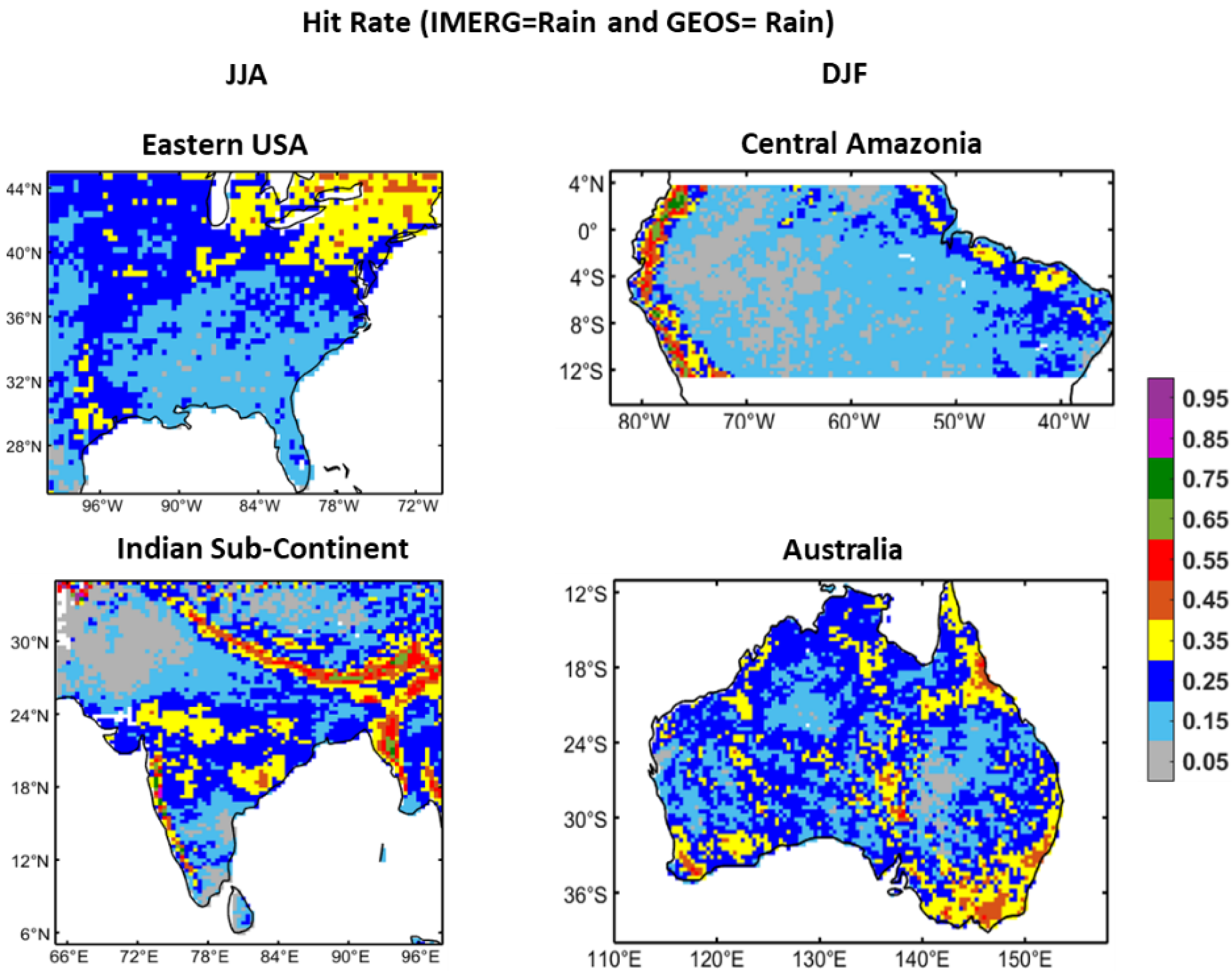

Figure 3(b): Spatial variability in hit rate (HR) in JJA over two regions in Northern Hemisphere (NH) i.e., Eastern USA, Indian sub-continent, and in DJF over Central Amazonia and Australia in Southern Hemisphere (SH) regions.

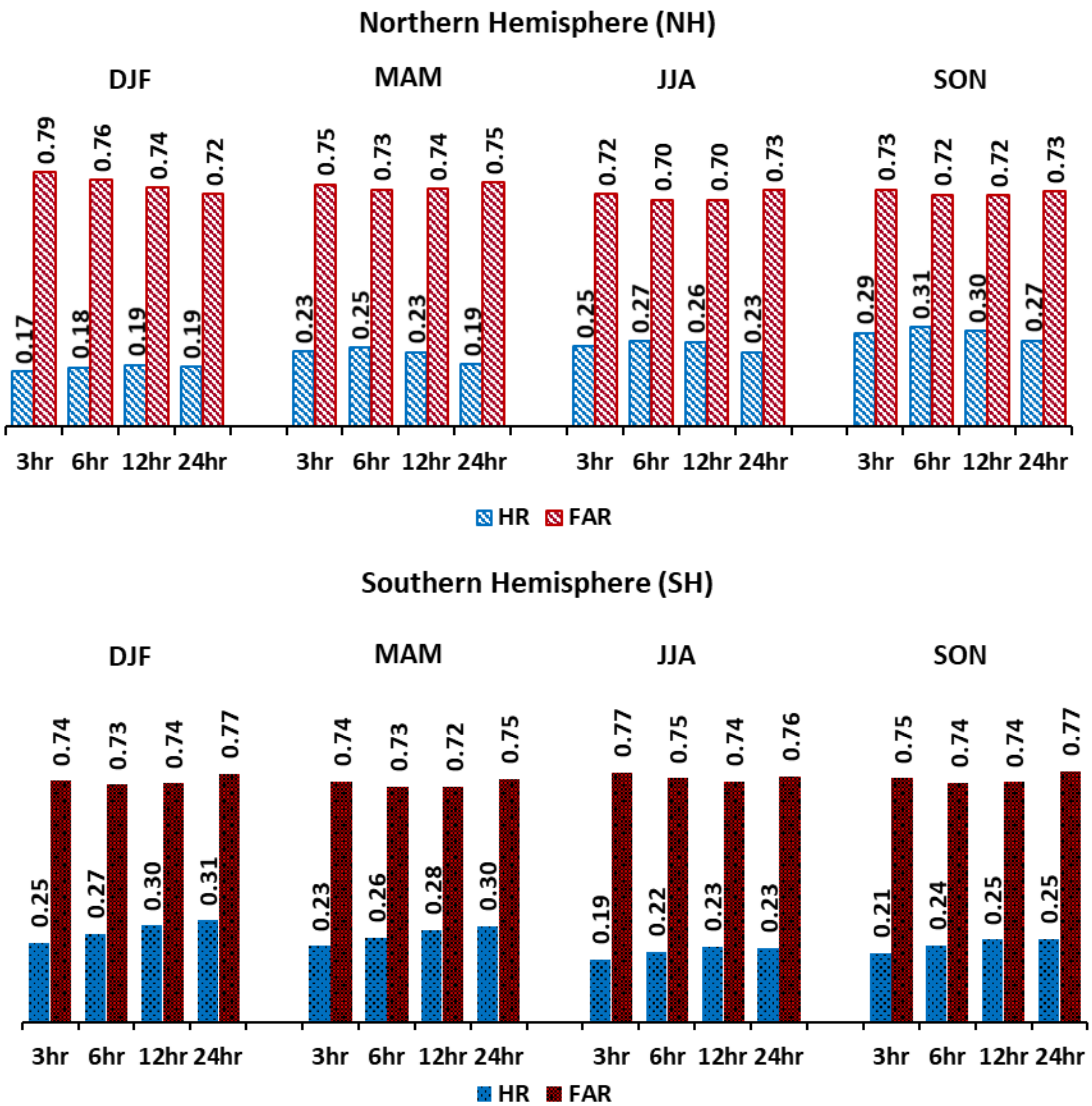

Figure 4: The Hit Rate (HR) and False Alarm Ratio (FAR) obtained over four different precipitation accumulation periods (3 hr, 6 hr, 12 hr, 24 hr) for Northern Hemisphere (Top) and Southern Hemisphere (Bottom).

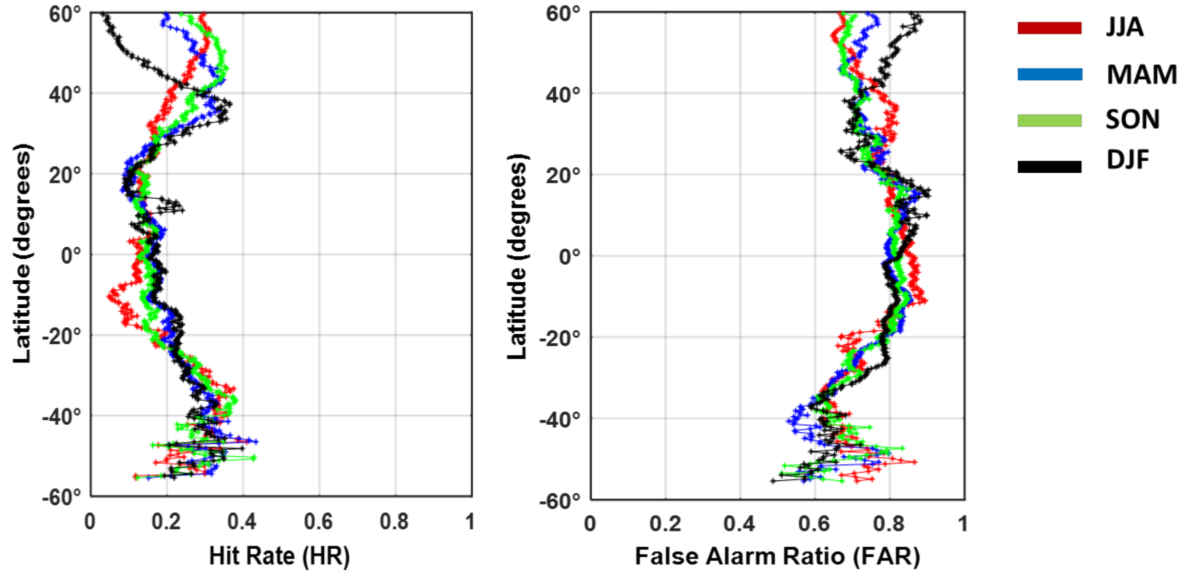

Figure 5: The latitudinal distribution in the Hit Rate (Left) and False Alarm Ratio (Right) plotted for four seasons; DJF, MAM, JJA, and SON.

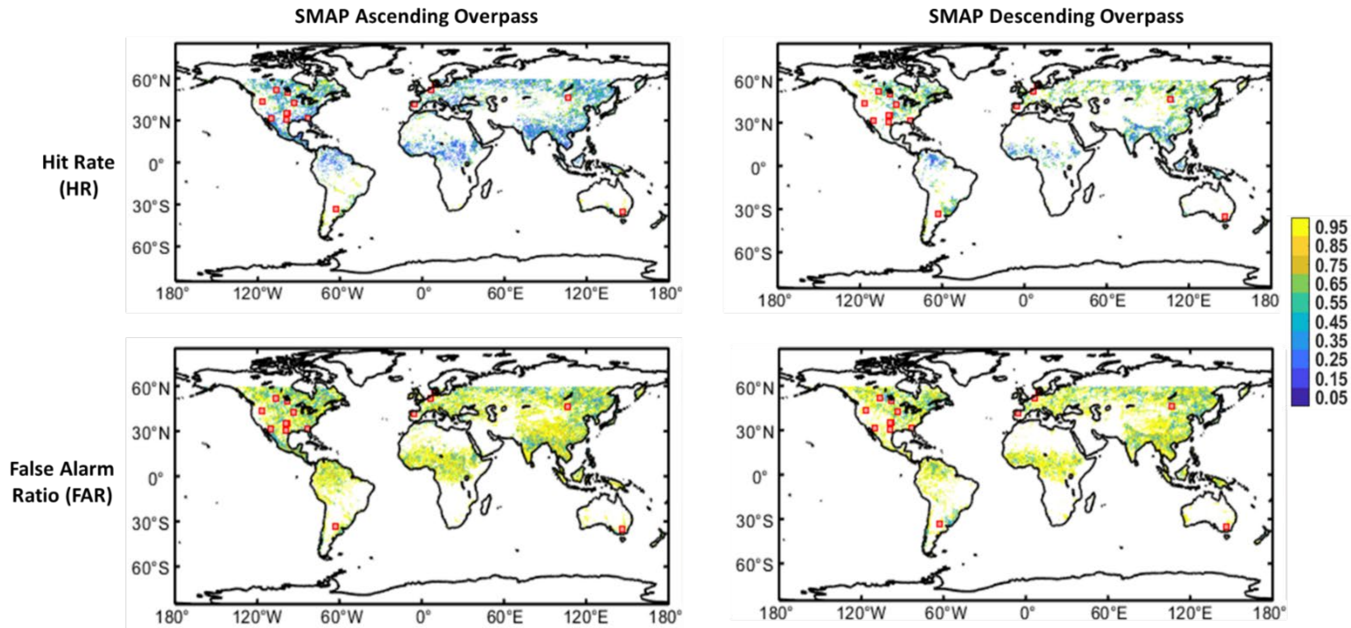

Figure 6: Global variations in the hit rate (HR) and false alarm ratio (FAR) observed for SMAP descending (6 AM) and ascending (6 PM) overpasses for June to August, 2018. The red squares represent the core validation sites (CVS).

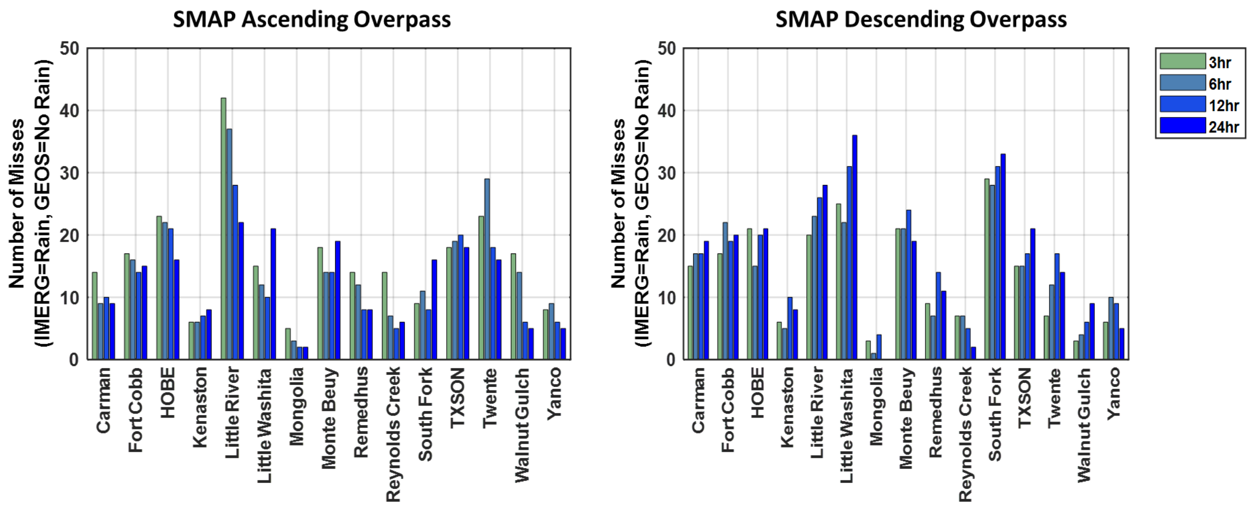

Figure 7(a): The variability in number of misdetections/misses for different precipitation accumulation periods for SMAP ascending (6 PM) (Left) and SMAP descending (6 AM) (Right) overpasses from April 2015- March 2020.

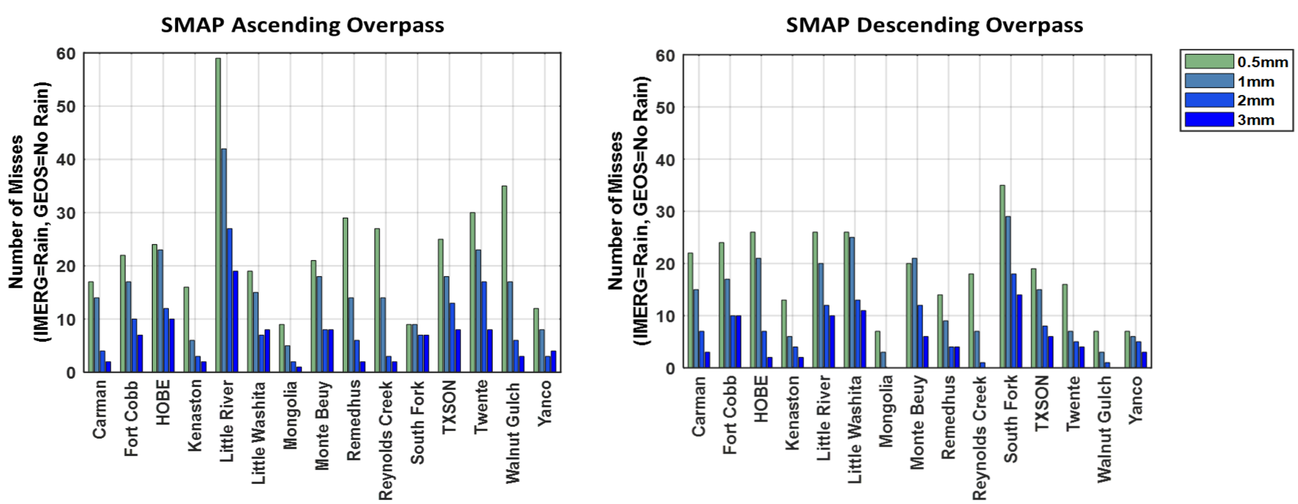

Figure 7(b): The variability in number of misdetections/misses for different precipitation thresholds for SMAP ascending (6 PM) (Left) and SMAP descending (6 AM) (Right) overpasses from April 2015- March 2020.

Table 1: The mean estimates of skill scores (Hit Rate = HR; False Alarm Ratio = FAR; Threat Score = TS; Gilbert Skill Score = GSS) are presented for 5 years (April, 2015 – March, 2020) of analysis, I) for GEOS-ARS, IMERG-ARS and GEOS-IMERG using three Agricultural Research Sites (ARS) which are also Core Validation Sites (CVS) for SMAP, II) seasonally for GEOS-IMERG for Northern Hemisphere (0°- 60°N), Southern Hemisphere (0°- 60°S), land-only pixels.

Table 1.I

Precipitation Accumulation	Data Sets	Little Washita				Fort Cobb				Little River			
		HR	FAR	TS	GS	HR	FAR	TS	GS	HR	FAR	TS	GS
3 hr	GEOS-ARS	0.26	0.72	0.14	0.16	0.22	0.76	0.12	0.13	0.11	0.85	0.05	0.07
	IMERG-ARS	0.32	0.75	0.14	0.16	0.30	0.77	0.14	0.15	0.17	0.87	0.06	0.08
	GEOS-IMERG	0.28	0.61	0.18	0.19	0.28	0.61	0.18	0.19	0.24	0.57	0.17	0.18
6 hr	GEOS-ARS	0.31	0.67	0.18	0.19	0.30	0.68	0.17	0.18	0.14	0.80	0.07	0.09
	IMERG-ARS	0.43	0.67	0.21	0.23	0.43	0.69	0.20	0.22	0.20	0.84	0.07	0.10
	GEOS-IMERG	0.33	0.55	0.22	0.24	0.33	0.50	0.23	0.25	0.25	0.53	0.18	0.20
12 hr	GEOS-ARS	0.36	0.62	0.21	0.23	0.37	0.58	0.23	0.25	0.20	0.71	0.12	0.14
	IMERG-ARS	0.57	0.56	0.31	0.33	0.55	0.56	0.30	0.32	0.37	0.71	0.17	0.19
	GEOS-IMERG	0.34	0.53	0.22	0.24	0.36	0.49	0.25	0.27	0.26	0.53	0.19	0.20

24 hr	GEOS-ARS	0.45	0.60	0.25	0.27	0.49	0.55	0.29	0.31	0.31	0.69	0.17	0.18
	IMERG-ARS	0.62	0.53	0.34	0.36	0.61	0.56	0.32	0.34	0.67	0.67	0.27	0.28
	GEOS-IMERG	0.38	0.54	0.24	0.26	0.41	0.46	0.28	0.30	0.26	0.45	0.20	0.22

Season	Precipitation Accumulation	Northern Hemisphere				Southern Hemisphere			
		HR	FAR	TS	GS	HR	FAR	TS	GS
DJF	3 hr	0.170	0.785	0.095	0.087	0.245	0.744	0.139	0.107
	6 hr	0.185	0.763	0.103	0.095	0.273	0.731	0.151	0.118
	12 hr	0.192	0.738	0.105	0.098	0.298	0.736	0.155	0.120
	24 hr	0.187	0.720	0.099	0.092	0.313	0.766	0.144	0.110
MAM	3 hr	0.232	0.749	0.127	0.117	0.234	0.741	0.135	0.112
	6 hr	0.246	0.733	0.133	0.122	0.260	0.726	0.148	0.123
	12 hr	0.231	0.736	0.125	0.114	0.283	0.725	0.154	0.127
	24 hr	0.194	0.754	0.100	0.090	0.296	0.748	0.144	0.118
JJA	3 hr	0.248	0.718	0.146	0.130	0.192	0.770	0.110	0.100
	6 hr	0.266	0.701	0.156	0.140	0.217	0.751	0.122	0.111
	12 hr	0.264	0.701	0.151	0.135	0.234	0.741	0.126	0.115
	24 hr	0.232	0.732	0.123	0.110	0.228	0.756	0.112	0.102

SON	3 hr	0.291	0.733	0.152	0.143	0.213	0.752	0.124	0.106
	6 hr	0.308	0.717	0.160	0.150	0.236	0.737	0.136	0.116
	12 hr	0.297	0.716	0.151	0.141	0.254	0.739	0.139	0.119
	24 hr	0.267	0.726	0.130	0.121	0.255	0.773	0.124	0.104

Table 2: Comparison between SMAP L2SMP soil moisture performance metrics (April, 2015 – March, 2020) estimated with (top row) and without (bottom row) accounting for misdetections based on 3 hr precipitation window for different IGBP land covers using CVS *in situ* stations soil moisture observations conducted for SMAP, *I)* ascending and *II)* descending orbits between April 2015 and March 2020 for Single Channel Algorithm (SCA-V).

Site Name	Location	Latitude, Longitude	Climate Regime	IGBP Land Cover	SCV- Ascending				
					ubRMSE (m^3/m^3)	Bias (m^3/m^3)	RMSE (m^3/m^3)	R	N
Remedhus	Spain	41.3° N, 5.4° W	Temperate	Croplands	0.039	0.007	0.039	0.831	693
					0.038	0.008	0.039	0.833	
Reynolds Creek	USA (Idaho)	31.72° N, 110.68° W	Arid	Grasslands	0.043	0.027	0.051	0.636	237
					0.043	0.028	0.051	0.639	
Yanco	Australia	34.8° S, 146.11° E	Semi-Arid	Croplands/Grasslands	0.041	-0.016	0.044	0.905	563
					0.039	-0.015	0.041	0.914	
Carman	Canada	49.62° N, 97.98° W	Cold	Croplands	0.061	0.065	0.090	0.574	308
					0.061	0.066	0.090	0.576	
Walnut Gulch	USA (Arizona)	31.72° N, 110.68° W	Arid	Shrub open	0.025	-0.012	0.027	0.765	471
					0.024	-0.011	0.027	0.768	
Little Washita	USA (Oklahoma)	34.97° N, 97.97° W	Temperate	Grasslands	0.022	0.011	0.024	0.913	442
					0.022	0.011	0.024	0.915	
Fort Cobb	USA (Oklahoma)	35.36° N, 98.55° W	Temperate	Grasslands	0.030	0.047	0.056	0.897	597
					0.030	0.047	0.056	0.897	
Little River	USA (Georgia)	31.64° N, 83.65° W	Temperate	Cropland/natural mosaic	0.037	-0.068	0.078	0.779	642
					0.037	-0.068	0.077	0.773	

South Fork	USA (Iowa)	42.44° N, 93.44°	Cold	Croplands	0.041	0.060	0.073	0.818	139
					0.042	0.060	0.073	0.805	
Monte Beuy	Argentina	32.96° S, 62.52° W	Arid	Croplands	0.040	0.000	0.040	0.882	325
					0.039	0.001	0.039	0.886	
Kenaston	Canada	50.45° N, 106.38° W	Cold	Croplands	0.026	0.000	0.026	0.882	285
					0.026	0.000	0.026	0.882	
TXSON	USA (Texas)	30.5° N, 98.5° W	Temperate	Grasslands	0.019	0.015	0.024	0.936	731
					0.019	0.015	0.024	0.937	
Mongolia	Mongolia	46.063° N,106.774° E	Cold	Grasslands	0.031	0.017	0.035	0.777	439
					0.031	0.017	0.035	0.773	

Site Name	Location	Latitude, Longitude	Climate Regime[II]	IGBP[III] Land Cover	SCV- Descending				
					ubRMSE (m^3 /m^3)	Bias (m^3 /m^3)	RMSE (m^3 /m^3)	R	N
Remedhus	Spain	41.3° N, 5.4° W	Temperate	Croplands	0.039	-0.006	0.040	0.830	544
					0.039	-0.006	0.040	0.830	
Reynolds Creek	USA (Idaho)	31.72° N, 110.68° W	Arid	Grasslands	0.040	0.021	0.045	0.667	170
					0.040	0.021	0.045	0.672	
Yanco	Australia	34.8° S, 146.11° E	Semi-Arid	Croplands/Grasslands	0.038	-0.018	0.042	0.902	530
					0.038	-0.018	0.042	0.903	
Carman	Canada	49.62° N, 97.98° W	Cold	Croplands	0.061	0.061	0.087	0.682	328
					0.061	0.061	0.087	0.677	
Walnut Gulch	USA (Arizona)	31.72° N, 110.68° W	Arid	Shrub open	0.027	-0.026	0.037	0.772	254
					0.027	-0.026	0.037	0.773	
Little Washita	USA (Oklahoma)	34.97° N, 97.97° W	Temperate	Grasslands	0.021	0.015	0.026	0.917	550
					0.021	0.015	0.026	0.916	
Fort Cobb	USA (Oklahoma)	35.36° N, 98.55° W	Temperate	Grasslands	0.029	0.046	0.054	0.896	652
					0.028	0.047	0.055	0.899	
Little River	USA (Georgia)	31.64° N, 83.65° W	Temperate	Cropland/natural mosaic	0.035	-0.066	0.075	0.800	715
					0.036	-0.066	0.075	0.797	
South Fork	USA (Iowa)	42.44° N, 93.44°	Cold	Croplands	0.045	0.053	0.070	0.742	349
					0.045	0.053	0.069	0.741	
Monte Beuy	Argentina	32.96° S, 62.52° W	Arid	Croplands	0.046	0.013	0.048	0.845	299
					0.045	0.013	0.047	0.846	
Kenaston	Canada	50.45° N, 106.38° W	Cold	Croplands	0.029	0.000	0.029	0.793	259
					0.029	0.000	0.029	0.793	
TXSON	USA (Texas)		Temperate	Grasslands	0.021	0.016	0.026	0.933	688

		30.5° N, 98.5° W			0.021	0.016	0.026	0.934	
Mongolia	Mongolia	46.063° N,106.774° E	Cold	Grasslands	0.039	0.009	0.040	0.766	110
					0.037	0.010	0.039	0.775	